Interactions and charge-transfer dynamics of an Al$^+$ ion immersed in ultracold Rb and Sr atoms

Michał Tomza * and Mateusz Lisaj

Faculty of Physics, University of Warsaw, Pasteura 5, 02-093 Warsaw, Poland

Atomic clocks based on an Al$^+$ ion sympathetically cooled by a laser-cooled alkaline-earth-metal ion have achieved unprecedented accuracy. Here, we investigate theoretically interactions and charge-transfer dynamics of an Al$^+$ ion immersed in an ultracold gas of Rb and Sr atoms. We calculate potential energy curves and transition electric dipole moments for the $(\mathrm{Al}+\mathrm{Rb})^+$ and $(\mathrm{Al}+\mathrm{Sr})^+$ ion-atom systems using coupled cluster and multireference configuration interaction methods with scalar relativistic effects included within the small-core energy-consistent pseudopotentials in Rb and Sr atoms. The long-range interaction coefficients are also reported. We use the electronic structure data to investigate cold collisions and charge-transfer dynamics. Scattering of an Al$^+$ ion with alkali-metal or alkaline-earth-metal atom is governed by one potential energy curve whereas charge transfer can lead to several electronic states mixed by the relativistic spin-orbit coupling. We examine the branching ratios resulting from the interplay of the short- and long-range effects, as well as the prospects for the laser-field control and formation of molecular ions. We propose to employ the atomic clock transition in an Al$^+$ ion to monitor ion-atom scattering dynamics *via* quantum logic spectroscopy. The presented results pave the way for the application of atomic ions other than alkali-metal and alkaline-earth-metal ones in the field of cold hybrid ion-atom experiments.

I. INTRODUCTION

Trapped and laser-cooled atomic ions allow for tackling questions touching upon the very fundamentals of quantum mechanics [1]. They have found many applications ranging from quantum simulation and quantum computation [2,3] to quantum metrology and sensing [4–6]. For example, optical atomic clocks based on single trapped ions have been realized [7–10]. Recently, the most stable and accurate single-ion atomic clock with fractional uncertainty as small as 10^{-18} has been constructed using the $^1S_0$ - $^3P_0$ transition in an Al$^+$ ion sympathetically cooled by a co-trapped and laser-cooled Mg$^+$ ion [11,12].

In the last decade, a new field of cold hybrid systems has emerged, where laser-cooled trapped ions are combined in a single experimental setup with ultracold atoms [13–15]. Ultracold atoms on their own have been used in numerous ground-breaking experiments allowing one to explore a plethora of quantum phenomena [16,17]. Mixtures of laser-cooled trapped ions and ultracold atoms may combine the best features of two well-established fields of research and promise new exciting applications in quantum physics and chemistry [15]. They can be employed to study cold collisions and sympathetic cooling [18–23], chemical reactions [24], spin and charge-transfer dynamics of ionic impurities [25–30], spin-controlled ion-atom chemistry [31], simulation of solid-state physics [32], and quantum computation [33]. Until now, most of the cold experiments have used alkaline-earth-metal

ions trapped and laser-cooled in Paul traps immersed into neutral alkali-metal or alkaline-earth-metal atoms trapped in magneto-optical, magnetic, or dipole traps. Investigated cold atomic combinations include the following: Yb$^+$/Yb [34], Ca$^+$/Rb [35], Ba$^+$/Ca [36], Yb$^+$/Ca [37], Yb$^+$/Rb [19], Ca$^+$/Li [38], Ca$^+$/Rb [39], Ca$^+$/Na [40], Yb$^+$/Li [41], Sr$^+$/Rb [42], Rb$^+$/Rb [20,43]. Additionally, sympathetically cooled molecular ions such as N$_2^+$ [24] and OH$^-$ [44] were immersed into ultracold Rb atoms. Recently, the direct formation of ions inside ultracold gases via the ionization of Rydberg states was also achieved [45–47].

In this paper, we propose to employ an Al$^+$ ion co-trapped in a Paul trap with a laser-cooled alkaline-earth-metal ion and overlapped with a small cloud of ultracold Rb or Sr atoms to investigate cold interactions and collisions, including charge-transfer dynamics, between an Al$^+$ ion and Rb or Sr atoms (see Fig. 1). Rb and Sr are selected as a prototype alkali-metal and alkaline-earth-metal atoms. Quantum state detection and preparation of the Al$^+$ ion may be realized by optical addressing of a co-trapped alkaline-earth-metal ion within the quantum logic spectroscopy [7]. Prospects for molecular ion formation are also analyzed. Scattering calculations are based on the electronic structure data, including potential energy curves and transition electric dipole moments, which we calculate using *ab initio* electronic structure approaches such as the coupled cluster and multireference configuration interaction methods.

The plan of this paper is as follows. Section II describes the used theoretical electronic structure and quantum scattering methods. Section III presents and analyzes the electronic and collisional properties of the investigated ion-atom systems. Section IV summarizes our paper and discusses future possible applications.
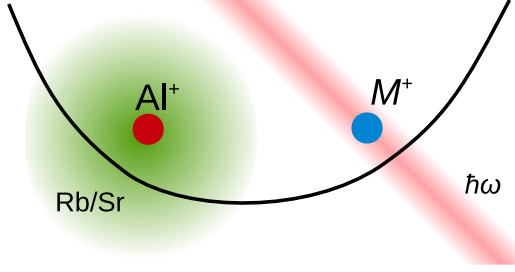
*michal.tomza@fuw.edu.pl

FIG. 1. Schematic representation of the considered experimental arrangement with an Al^+ ion co-trapped in a Paul trap with a laser-cooled alkaline-earth-metal ion M^+. An Al^+ ion is overlapped with a small cloud of ultracold Rb or Sr atoms, whereas an alkaline-earth-metal ion is optically addressed to control and read a quantum state of both ions.

II. COMPUTATIONAL DETAILS

An Al^+ ion has a closed-shell electronic ground state of the $^1S_0$ symmetry. Its interaction with a ground-state alkali-metal (alkaline-earth-metal) atom in the $^2S_{1/2}$ ($^1S_0$) electronic state results in a single molecular electronic state of the $^2\Sigma^+$ ($^1\Sigma^+$) symmetry. The ionization potential of an Al atom is larger than of all alkali-metal atoms and of Sr and Ba among alkaline-earth-metal atoms, therefore the charge-transfer process is energetically possible in collisions between an Al^+ ion and those atoms [48]. Interestingly, such a process leads to several electronic states dissociating to the lowest ion-atom asymptotes with an Al atom in the $^2P_{1/2}$ or $^2P_{3/2}$ electronic state. In the nonrelativistic picture, if an Al atom interacts with an alkali-metal ion then two molecular electronic states of the $^2\Sigma^+$ and $^2\Pi$ symmetries exist, and if an Al atom interacts with an alkaline-earth-metal ion then four molecular electronic states of the $^1\Sigma^+$, $^1\Pi$, $^3\Sigma^+$, and $^3\Pi$ symmetries are possible. Relativistic effects, namely the spin-orbit coupling which splits the atomic ^2P electronic state into the $^2P_{1/2}$ and $^2P_{3/2}$ fine states, couple and mix different molecular electronic states. Relativistic effects, which are of moderate values in the considered systems, can be included perturbatively [49,50].

To calculate potential energy curves in the Born-Oppenheimer approximation we adopt the computational scheme successfully applied to the ground and excited electronic states of the $(LiYb)^+$ molecular ion [51] and SrYb molecule [49]. The nonrelativistic potential energy curves are obtained using the multireference configuration interaction method restricted to single and double excitations with the Davidson correction, MRCISD+Q, starting from orbitals obtained with the multiconfigurational self-consistent field method (MCSCF) [52]. Complete active spaces constructed from $3s3p$, $5s5p$, and $5s5p4d$ atomic orbitals of Al, Rb, and Sr are used. When possible the spin-restricted open-shell coupled cluster method restricted to single, double, and noniterative triple excitations, starting from the restricted open-shell Hartree-Fock (ROHF) orbitals, RCCSD(T), is employed [53]. The interaction energies are obtained with the supermolecular method with the basis set superposition error corrected by using the counterpoise correction [54],

$$V_{(Al+X)^+} = E_{(Al+X)^+} - E_{Al^+} - E_X, \quad (1)$$

where $E_{(Al+X)^+}$ is the total energy of the ion-atom system, and E_{Al^+} and E_X are the total energies of the Al^+ ion and X atom computed in the diatom basis set.

The Al atom is described by the augmented correlation consistent polarized valence and core-valence quintuple-ζ quality basis sets, aug-cc-pV5Z (in MRCISD+Q calculations) and aug-cc-pCV5Z (in RCCSD(T) calculations), respectively [55]. The scalar relativistic effects in Rb and Sr atoms are included by employing the small-core relativistic energy-consistent pseudopotentials (ECP) to replace the inner-shell electrons [56]. The pseudopotentials from the Stuttgart library are employed in all calculations. The Rb and Sr atoms are described with the ECP28MDF pseudopotentials [57,58] together with the $[14s14p7d6f1g]$ and $[14s11p6d5f4g]$ basis sets reported in Refs. [49,59]. The atomic basis sets are additionally augmented in all calculations by the set of $[3s3p2d1f1g]$ bond functions to accelerate the convergence towards the complete basis set limit [60]. All electronic structure calculations are performed with the MOLPRO package of *ab initio* programs [61].

The relativistic potential energy curves $V_{|\Omega|}(R)$ associated with the two lowest atomic asymptotes of the $Al(^2P_J)$ atom interacting with the $Rb^+(^1S_0)$ or $Sr^+(^2S_{1/2})$ ion are obtained within the perturbation theory by diagonalizing the interaction Hamiltonians with the spin-orbit coupling included between nonrelativistic curves. Relativistic states are characterized by the projection of the total angular momentum on the molecular axis $|\Omega|$.

For $Al(^2P_J) + Rb^+(^1S_0)$, the relativistic molecular potential energy curves are given by

$$V_{|\Omega|=\frac{1}{2}}(R) = \begin{pmatrix} V_{^2\Sigma}(R) & A_{SO}^{^2\Sigma/^2\Pi}(R) \\ A_{SO}^{^2\Sigma/^2\Pi}(R) & V_{^2\Pi}(R) - A_{SO}^{^2\Pi/^2\Pi}(R) \end{pmatrix}, \quad (2)$$

$$V_{|\Omega|=\frac{3}{2}}(R) = V_{^2\Pi}(R) + A_{SO}^{^2\Pi/^2\Pi}(R), \quad (3)$$

where $V_{^{2S+1}|\Lambda|}(R)$ is the nonrelativistic potential energy curve for the $^{2S+1}|\Lambda|$ electronic state and $A_{SO}^{^{2S+1}|\Lambda|/^{2S'+1}|\Lambda'|}(R)$ is the matrix element of the spin-orbit coupling Hamiltonian, $\hat{H}_{SO} = \hat{S} \cdot \hat{L}$, between the $^{2S+1}|\Lambda|$ and $^{2S'+1}|\Lambda'|$ electronic states [62].

For $Al(^2P_J) + Sr^+(^2S_{1/2})$, the relativistic molecular potential energy curves are given by

$$V_{|\Omega|=0^+}(R) = \begin{pmatrix} V_{^1\Sigma}(R) & A_{SO}^{^1\Sigma/^3\Pi}(R) \\ A_{SO}^{^1\Sigma/^3\Pi}(R) & V_{^3\Pi}(R) - A_{SO}^{^3\Pi/^3\Pi}(R) \end{pmatrix}, \quad (4)$$

$$V_{|\Omega|=1}(R) = \begin{pmatrix} V_{^3\Sigma}(R) & A_{SO}^{^3\Sigma/^3\Pi}(R) & A_{SO}^{^3\Sigma/^1\Pi}(R) \\ A_{SO}^{^3\Sigma/^3\Pi}(R) & V_{^3\Pi}(R) & -A_{SO}^{^3\Pi/^1\Pi}(R) \\ A_{SO}^{^3\Sigma/^1\Pi}(R) & -A_{SO}^{^3\Pi/^1\Pi}(R) & V_{^1\Pi}(R) \end{pmatrix}, \quad (5)$$

$$V_{|\Omega|=2}(R) = V_{^3\Pi}(R) + A_{SO}^{^3\Pi/^3\Pi}(R). \quad (6)$$

Asymptotically, the spin-orbit coupling matrix elements are related to the fine splitting between $^2P_{1/2}$ and $^2P_{3/2}$ electronic states of the Al atom $\Delta E_{fs}^{Al} = 112.1\,cm^{-1}$ [63]. $A_{SO}^{^2\Pi/^2\Pi}(R \to \infty) = A_{SO}^{^3\Sigma/^3\Pi}(R \to \infty) = A_{SO}^{^3\Sigma/^1\Pi}(R \to \infty) = A_{SO}^{^3\Pi/^1\Pi}(R \to \infty) = \Delta E_{fs}^{Al}/3$ and $A_{SO}^{^2\Sigma/^2\Pi}(R \to \infty) =$

$A_{\mathrm{SO}}^{^1\Sigma/^3\Pi}(R \to \infty) = \sqrt{2}\Delta E_{\mathrm{fs}}^{\mathrm{Al}}/3$. In the present study, we neglect the R dependence of the matrix elements of the spin-orbit coupling assuming their asymptotic values. This approximation should not significantly affect the presented results dominated by the dynamics at intermediate- and long-range distances.

The interaction potential between the ion and the atom at large internuclear distances R is generally given by

$$V_{(\mathrm{Al}+X)^+}(R) = -\frac{C_3^{\mathrm{elst}}}{R^3} - \frac{C_4^{\mathrm{ind}}}{R^4} - \frac{C_6^{\mathrm{ind}}}{R^6} - \frac{C_6^{\mathrm{disp}}}{R^6} + \ldots, \quad (7)$$

where $-C_3^{\mathrm{elst}}/R^3$ term describes the electrostatic interaction between the charge of the ion and the permanent quadrupole moment of the atom with nonzero electronic angular momentum ($L \neq 0$), $-C_4^{\mathrm{ind}}/R^4 - C_6^{\mathrm{ind}}/R^6$ terms describe the induction interaction between the charge of the ion and the induced electric dipole and quadruple moments of the atom, respectively, and $-C_6^{\mathrm{disp}}/R^6$ term describes the dispersion interaction between instantaneous dipole-induced dipole moments of the ion and atom arising due to quantum fluctuations [64].

The leading long-range interaction coefficients do not depend on the total electronic spin of molecular electronic states and for Σ and Π symmetries they are given by

$$C_3^{\mathrm{elst}}(\Sigma) = q\Theta_{\mathrm{at}},$$

$$C_3^{\mathrm{elst}}(\Pi) = -\frac{1}{2}q\Theta_{\mathrm{at}},$$

$$C_4^{\mathrm{ind}}(\Sigma) = \frac{1}{2}q^2\left(\bar{\alpha}_{\mathrm{at}} + \frac{2}{3}\Delta\alpha_{\mathrm{at}}\right),$$

$$C_4^{\mathrm{ind}}(\Pi) = \frac{1}{2}q^2\left(\bar{\alpha}_{\mathrm{at}} - \frac{1}{3}\Delta\alpha_{\mathrm{at}}\right),$$

$$C_6^{\mathrm{ind}}(\Sigma) = \frac{1}{2}q^2\left(\bar{\beta}_{\mathrm{at}} + \frac{2}{3}\Delta\beta_{\mathrm{at}}\right), \quad \quad (8)$$

$$C_6^{\mathrm{ind}}(\Pi) = \frac{1}{2}q^2\left(\bar{\beta}_{\mathrm{at}} - \frac{1}{3}\Delta\beta_{\mathrm{at}}\right),$$

$$C_6^{\mathrm{disp}}(\Sigma) = \frac{3}{\pi}\int_0^\infty \alpha_{\mathrm{ion}}(i\omega)\left(\bar{\alpha}_{\mathrm{at}}(i\omega) + \frac{2}{3}\Delta\alpha_{\mathrm{at}}(i\omega)\right)d\omega,$$

$$C_6^{\mathrm{disp}}(\Pi) = \frac{3}{\pi}\int_0^\infty \alpha_{\mathrm{ion}}(i\omega)\left(\bar{\alpha}_{\mathrm{at}}(i\omega) - \frac{1}{3}\Delta\alpha_{\mathrm{at}}(i\omega)\right)d\omega,$$

where q is the charge of the ion, Θ_{at} is the permanent quadrupole moment of the atom, $\bar{\alpha}_{\mathrm{at}} = (\alpha_{xx} + \alpha_{yy} + \alpha_{zz})/3$ and $\Delta\alpha_{\mathrm{at}} = \alpha_{zz} - \alpha_{xx}$ are the isotropic (scalar) and anisotropic (tensor) components of the static electric dipole polarizability of the atom, $\bar{\beta}_{\mathrm{at}}$ and $\Delta\beta_{\mathrm{at}}$ are the components of the static electric quadrupole polarizability of the atom, and $\bar{\alpha}_{\mathrm{ion(atom)}}(i\omega)$ and $\Delta\alpha_{\mathrm{ion(atom)}}(i\omega)$ are the components of the dynamic polarizability of the ion(atom) at imaginary frequency. The permanent quadrupole moment and static quadrupole polarizability of the Al atom are calculated with the RCCSD(T) and finite field methods. The dynamic electric dipole polarizabilities at imaginary frequency of the Rb and Sr atoms are taken from Ref. [65], whereas the dynamic polarizability of the Al$^+$ and Rb$^+$ ions are obtained by using the explicitly connected representation of the expectation value and polarization propagator within the coupled cluster method [66]. The dynamic
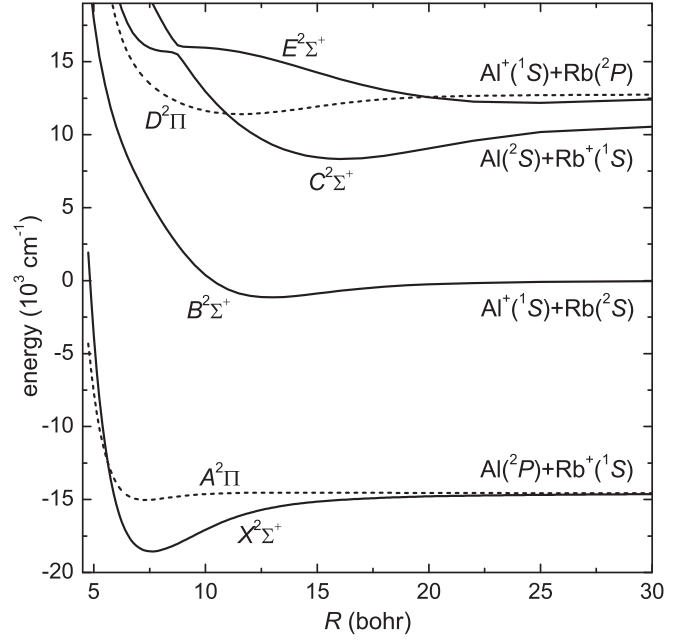

FIG. 2. Nonrelativistic molecular potentials energy curves of the $(\mathrm{Al} + \mathrm{Rb})^+$ ion-atom system.

polarizabilities of the Sr$^+$ ion and the Al atom are obtained from the sum over state expression using the transition moments and energy levels from the NIST Atomic Spectra Database [63].

Rate constants for elastic scattering and inelastic charge-exchange reactive collisions are calculated as implemented and described in Refs. [48,51,67]. The time-independent Schrödinger equation for the nuclear motion of colliding ion and atom is solved using the renormalized Numerov propagator [68] with step-size doubling. The wave functions are propagated to large interatomic separations and the K and S matrices are extracted by imposing the long-range scattering boundary conditions in terms of the Bessel functions. The elastic rate constants and scattering lengths are obtained from the S matrix for the entrance channel, while inelastic rate constants are calculated using Fermi golden rule type expressions based on Einstein coefficients between bound and continuum ro-vibrational wave functions of relevant electronic states. We neglect the hyperfine structure of Rb, Al, and Sr$^+$ because it should be negligible for the scattering dynamics in the entrance channels, while studying interplay of the fine and hyperfine structures in the exit channels is out of the scope of this paper.

III. NUMERICAL RESULTS AND DISCUSSION

A. Potential energy curves and transition electric dipole moments

Figures 2 and 3 present nonrelativistic molecular potential energy curves for the ground and excited electronic states of the $(\mathrm{Al} + \mathrm{Rb})^+$ and $(\mathrm{Al} + \mathrm{Sr})^+$ ion-atom systems, respectively. Their spectroscopic characteristics, such as equilibrium bond lengths R_e, well depths D_e, harmonic constants ω_e, and rotational constants B_e, are collected in Tables I and II.
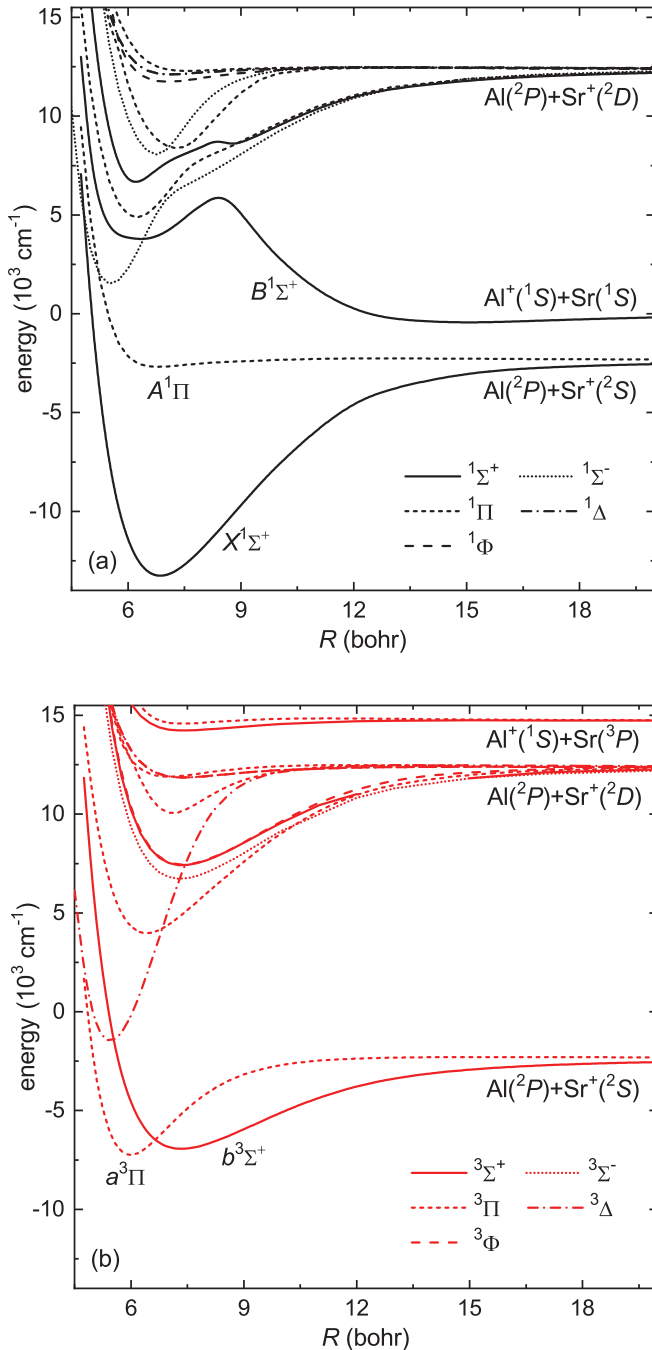
FIG. 3. Nonrelativistic singlet (a) and triplet (b) molecular potentials energy curves of the $(Al + Sr)^+$ ion-atom system.

TABLE I. Spectroscopic characteristics of molecular electronic states of the $(^{27}Al + {}^{85}Rb)^+$ ion-atom system: equilibrium bond lengths R_e, well depths D_e, harmonic constants ω_e, and rotational constants B_e. Results obtained with the couple-cluster (CC) and configuration interaction (CI) methods are presented as described in the text.

State	Met.	R_e (bohr)	D_e (cm^{-1})	ω_e (cm^{-1})	B_e (cm^{-1})
		$Al(^2P) + Rb^+(^1S)$			
$X\ ^2\Sigma^+$	CC	7.59	3971	85.3	0.0510
$X\ ^2\Sigma^+$	CI	7.66	3940	83.3	0.0502
$A\ ^2\Pi$	CC	7.31	443	56.9	0.0550
$A\ ^2\Pi$	CI	7.35	395	55.5	0.0544
		$Al^+(^1S) + Rb(^2S)$			
$B\ ^2\Sigma^+$	CI	12.91	1158	34.6	0.0176
		$Al(^2S) + Rb^+(^1S)$			
$C\ ^2\Sigma^+$	CI	16.13	2425	30.0	0.0113
		$Al^+(^1S) + Rb(^2P)$			
$D\ ^2\Pi$	CI	11.56	1327	29.6	0.0220
$E\ ^2\Sigma^+$	CI	24.24	559	13.2	0.00501

nonadiabatic radial couplings [37,69,70], will be suppressed and negligible as compared to the radiative charge transfer, which is driven by the transition electric dipole moments. The spontaneous radiative transitions to the electronic states related to the $Al(^2P) + Rb^+(^1S)$ atomic threshold can result in the radiative charge transfer or the radiative association depending on the structure of potential energy curves and transition electric dipole moments. In the case of the $(Al + Rb)^+$ system, as shown in Fig. 4, the transition moment between the $B\ ^2\Sigma^+$ and $X\ ^2\Sigma^+$ electronic states is noticeably larger than the one between the $B\ ^2\Sigma^+$ and $A\ ^2\Pi$ states, in favor of radiative processes leading to the $X\ ^2\Sigma^+$ state. The equilibrium distance of the $B\ ^2\Sigma^+$ state is larger as compared to the $X\ ^2\Sigma^+$ and $A\ ^2\Pi$ states but some overlap between vibrational states associated with these electronic states can be expected.

The electronic structure of the $(Al + Sr)^+$ system, presented in Fig. 3, is noticeably more complex as compared to the $(Al + Rb)^+$ system due to one electron more in the valence shell of the Sr atom. Thus, two families of singlet and triplet molecular electronic states of the $^1\Sigma^+$, $^1\Sigma^-$, $^1\Pi$, $^1\Delta$, $^1\Phi$ and $^3\Sigma^+$, $^3\Sigma^-$, $^3\Pi$, $^3\Delta$, $^3\Phi$ symmetries are relevant in the present study. The $Al(^2P) + Sr^+(^2D)$ atomic threshold is related with the richest family of 18 different nonrelativistic molecular electronic states. The inclusion of the relativistic spin-orbit coupling would further increase the number of molecular electronic states and complexity of the system. The entrance $B\ ^1\Sigma^+$ electronic state is separated from higher lying electronic states, but its $Al^+(^1S) + Sr(^1S)$ atomic threshold is just 2346 cm^{-1} above the lowest $Al(^2P) + Sr^+(^2S)$ atomic threshold. This suggests that nonradiative charge transfer driven by the nonadiabatic radial couplings can compete with the radiative charge transfer in this case. In the case of the $(Al + Sr)^+$ system, as shown in Fig. 5, the transition moment between the $B\ ^1\Sigma^+$ and $X\ ^1\Sigma^+$ electronic

Figures 4 and 5 show the transition electric dipole moments between the ground and excited molecular electronic states of the $(Al + Rb)^+$ and $(Al + Sr)^+$ ion-atom systems, respectively. The calculated electronic structure data are available in numerical form from the authors upon request.

All relevant nonrelativistic molecular electronic states of the $(Al + Rb)^+$ system, presented in Fig. 2, are of the $^2\Sigma^+$ or $^2\Pi$ symmetry. The entrance $B\ ^2\Sigma^+$ electronic state, related to the $Al^+(^1S) + Rb(^2S)$ atomic threshold, is well separated from lower and higher lying electronic states. This suggests that nonradiative charge transfer, which could be driven by the

TABLE II. Spectroscopic characteristics of molecular electronic states of the $(^{27}\text{Al} + {}^{88}\text{Sr})^+$ ion-atom system: equilibrium bond lengths R_e, well depths D_e, harmonic constants ω_e, and rotational constants B_e. Results obtained with the couple-cluster (CC) and configuration interaction (CI) methods are presented as described in the text.

State	Met.	R_e (bohr)	D_e (cm^{-1})	ω_e (cm^{-1})	B_e (cm^{-1})
		$\text{Al}(^2P) + \text{Sr}^+(^2S)$			
$X\ ^1\Sigma^+$	CC	6.84	10 949	142.2	0.0628
$X\ ^1\Sigma^+$	CI	7.07	9763	131.5	0.0582
$a\ ^3\Pi$	CC	6.00	4897	180.2	0.0818
$a\ ^3\Pi$	CI	6.26	3951	165.9	0.0745
$b\ ^3\Sigma^+$	CC	7.35	4586	89.0	0.0545
$b\ ^3\Sigma^+$	CI	7.51	3964	79.7	0.0521
$A\ ^1\Pi$	CI	6.77	341	67.6	0.0602
		$\text{Al}^+(^1S) + \text{Sr}(^1S)$			
$B\ ^1\Sigma^+$	CI	14.55	499	26.0	0.0140
		$\text{Al}(^2P) + \text{Sr}^+(^2D)$			
$(3)\ ^1\Sigma^+$	CI	6.17	5796	213.1	0.0765
$(1)^1\Sigma^-$	CI	5.54	10 894	233.8	0.0951
$(2)^1\Sigma^-$	CI	6.75	4324	195.4	0.0640
$(2)\ ^1\Pi$	CI	6.22	7521	176.5	0.0753
$(3)\ ^1\Pi$	CI	7.30	4015	134.1	0.0547
$(4)\ ^1\Pi$	CI	7.57	106	44.4	0.0509
$(1)\ ^1\Delta$	CI	7.11	287	60.5	0.0576
$(2)\ ^1\Delta$	CI		repulsive		
$(1)\ ^1\Phi$	CI	7.02	660	69.9	0.0591
$(2)\ ^3\Sigma^+$	CI	7.36	4985	95.3	0.0539
$(1)^3\Sigma^-$	CI	7.31	5664	99.1	0.0546
$(2)^3\Sigma^-$	CI	7.40	548	56.4	0.0533
$(2)\ ^3\Pi$	CI	6.40	8456	141.0	0.0713
$(3)\ ^3\Pi$	CI	7.11	2345	141.7	0.0578
$(4)\ ^3\Pi$	CI	7.00	511	74.8	0.0595
$(1)\ ^3\Delta$	CI	5.44	13 969	256.4	0.0983
$(2)\ ^3\Delta$	CI		repulsive		
$(1)\ ^3\Phi$	CI	7.39	4951	95.3	0.0537
		$\text{Al}^+(^1S) + \text{Sr}(^3P)$			
$(4)\ ^3\Sigma^+$	CI	7.38	474	54.0	0.0535
$(5)\ ^3\Pi$	CI	7.34	128	54.8	0.0541

states is also noticeably larger than the one between the $B\ ^1\Sigma^+$ and $A\ ^1\Pi$ states, in favor of radiative processes leading to the $X\ ^1\Sigma^+$ state. The equilibrium distance of the $B\ ^1\Sigma^+$ state is much larger as compared to the $X\ ^1\Sigma^+$ and $A\ ^1\Pi$ states, hence a small overlap between vibrational states associated with these electronic states may be expected. Excited electronic states have equilibrium distances and well depths in a broad range of values.

The long-range electrostatic, induction, and dispersion interaction coefficients describing the long-range part of the interaction potential energy curves between the Al^+ ion and
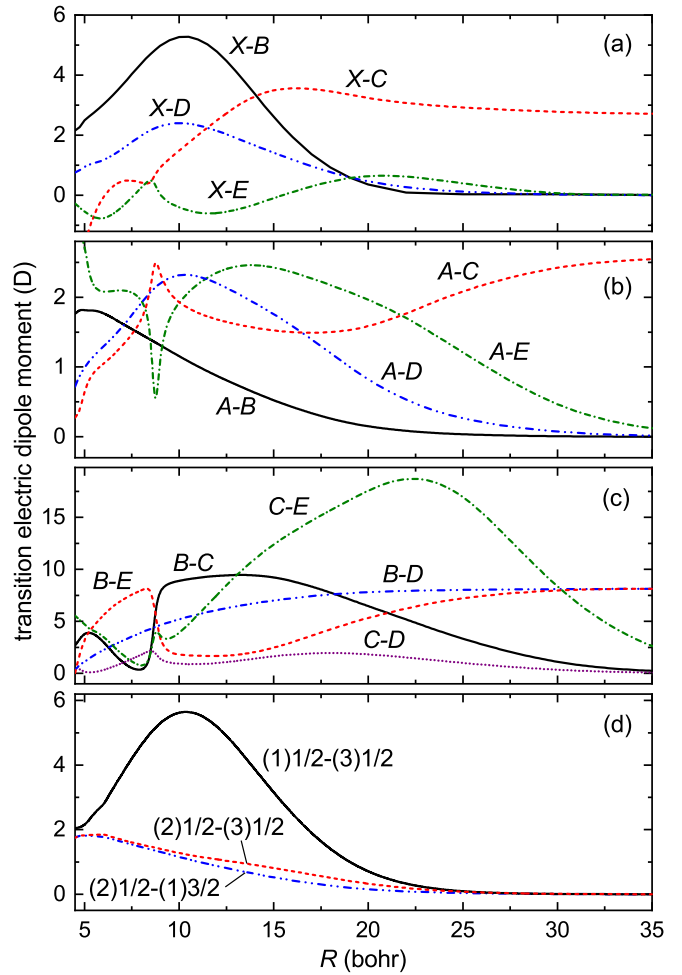

FIG. 4. Transition electric dipole moments between the ground and excited molecular electronic states of the $(\text{Al} + \text{Rb})^+$ ion-atom system. Panels (a)–(c) are for transitions between nonrelativistic states and panel (d) is for transitions between relativistic states.

the Rb or Sr atom and between the Rb$^+$ or Sr$^+$ ion and the Al atom are collected in Table III. They are based on the electronic properties of monomers calculated in the present study: the static electric dipole and quadruple polarizabilities of the Rb and Sr atoms $\bar{\alpha}_{\text{Rb}} = 319.5$ a.u., $\bar{\alpha}_{\text{Sr}} = 199.2$ a.u., $\bar{\beta}_{\text{Rb}} = 6578$ a.u., $\bar{\beta}_{\text{Sr}} = 4551$ a.u., the isotropic and anisotropic com-

TABLE III. Electrostatic, induction, and dispersion interaction coefficients (in atomic units) describing the long-range part of the interaction potentials between the Al$^+$ ion and the Rb or Sr atom and between the Rb$^+$ or Sr$^+$ ion and the Al atom, all in the ground electronic state.

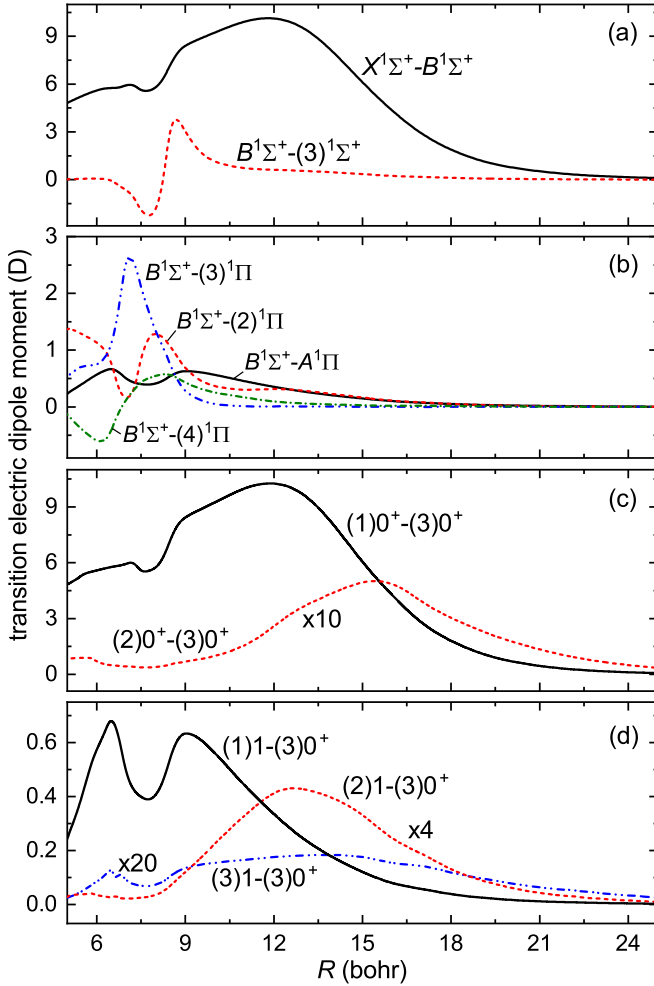| System	Sym.	C_3^{el}	C_4^{ind}	C_6^{ind}	C_6^{disp}
$\text{Al}^+(^1S) + \text{Rb}(^2S)$	$^2\Sigma$	–	159.8	3346	615
$\text{Al}(^2P) + \text{Rb}^+(^1S)$	$^2\Sigma$	5.20	37.3	414	106
$\text{Al}(^2P) + \text{Rb}^+(^1S)$	$^2\Pi$	−2.60	24.6	260	70
$\text{Al}^+(^1S) + \text{Sr}(^1S)$	$^1\Sigma$	–	99.6	2311	567
$\text{Al}(^2P) + \text{Sr}^+(^2S)$	$^1\Sigma, {}^3\Sigma$	5.20	37.3	414	578
$\text{Al}(^2P) + \text{Sr}^+(^2S)$	$^1\Pi, {}^3\Pi$	−2.60	24.6	260	381

FIG. 5. Transition electric dipole moments between selected ground and excited molecular electronic states of the $(Al + Sr)^+$ ion-atom system. Panels (a) and (b) are for transitions between nonrelativistic states and panels (c) and (d) are for transitions between relativistic states.

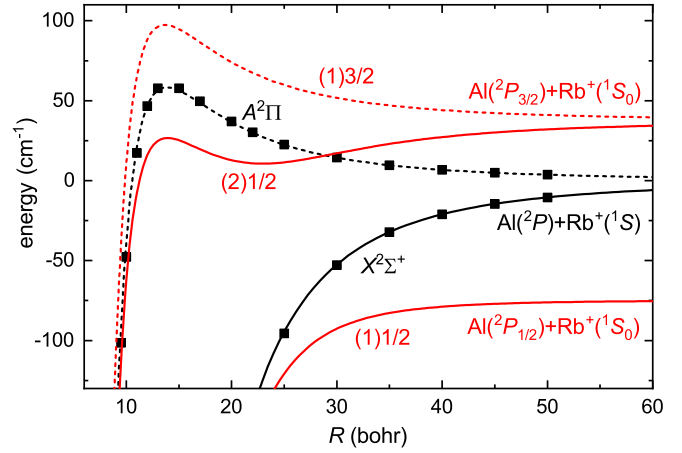FIG. 6. The long-range part of the interaction potentials for the $(Al + Rb)^+$ ion-atom system. Points are the result of the supermolecular calculations and lines are the multipole expansion $-C_3/R^3 - C_4/R^4 - C_6/R^6$ with coefficients obtained within the perturbation theory. Black and red (gray) lines present nonrelativistic and relativistic potential energy curves, respectively.

ponents of the electric dipole and quadruple polarizabilities of the Al atom $\bar{\alpha}_{Al} = 57.7$ a.u., $\Delta\alpha_{Al} = 25.4$ a.u., $\bar{\beta}_{Al} = 622$ a.u., $\Delta\beta_{Al} = 309$ a.u., the electric quadruple moment of the Al atom $\Theta_{Al} = 5.2$ a.u., and the static electric dipole polarizabilities of the Al^+, Rb^+, and Sr^+ ions, $\bar{\alpha}_{Al^+} = 24.2$ a.u., $\bar{\alpha}_{Rb^+} = 9.2$ a.u., $\bar{\alpha}_{Sr^+} = 92.0$ a.u. These values agree well with previous measurements and calculations [71].

An additional check of the accuracy of the employed *ab initio* methods is a comparison of the ionization potentials and atomic excitation energies with experimental values. The calculated ionization potentials of the Al, Rb, and Sr atoms are 48 123 cm^{-1}, 33 566 cm^{-1}, and 45 814 cm^{-1}. They agree within 0.5% with experimental values of 48 278 cm^{-1}, 33 691 cm^{-1}, and 45 932 cm^{-1} [63]. The lowest nonrelativistic excitation energies of the Al, Rb, Sr atoms are 25 388 cm^{-1}, 12 686 cm^{-1}, and 14 639 cm^{-1}. They also agree within 0.5% with corresponding experimental values of 25 273 cm^{-1}, 12 737 cm^{-1}, and 14 705 cm^{-1} [63]. The lowest computed excitation energy for the Sr^+ ion is 15 370 cm^{-1} as compared to experimental value of 14 724 cm^{-1}.

Finally, the uncertainty of the calculated potential energy curves and electronic properties is of the order of 5%–15% depending on the electronic state. This estimation is based on the analysis of the convergence with the size of the used atomic basis sets and the level of employed theory. The lack of the exact treatment of the triple and higher excitations in the employed CCSD(T) and MRCISD methods, infeasible computationally to include for the studied systems, is a primary limiting factor. The presented CCSD(T) and MRCISD results agree with each other within about 10 %.

The long-range part of the interaction potential is especially important for cold and ultracold collisions, when shape resonances, and quantum reflection and tunneling play a role. Figure 6 presents the long-range part of the interaction potentials for the lowest asymptote of the $(Al + Rb)^+$ ion-atom system obtained in the molecular nonrelativistic calculations together with the interaction potentials given by the multipole expansion of Eq. (7) obtained within the perturbation theory. Both approaches agree well in a broad range of interatomic distances. This agreement additionally validates the employed electronic structure methods and results from the size consistency of the coupled cluster method combined with the same level of theory used to describe dimer and monomers. Similar agreement is achieved for the $(Al + Sr)^+$ ion-atom system. Additionally, the impact of the spin-orbit coupling in the $(Al + Rb)^+$ system is presented by showing the relativistic potential energy curves connected to two fine-state manifolds obtained by the diagonalization of Eqs. (2) and (3).

The leading long-range induction interaction given by the C_4 coefficient for the Al^+ ion interacting with the Rb or Sr atom determines the characteristic interaction length scale $R_4 = \sqrt{2\mu C_4/\hbar^2}$ and the related energy scale $E_4 = \hbar^2/2\mu R_4^2$ relevant for ultracold ion-atom collisions [15]. For the $Al^+ + Rb$ and $Al^+ + Sr$ systems they take values of $R_4 = 3454$ bohr, $E_4 = 355$ nK and $R_4 = 2738$ bohr, $E_4 = 560$ nK, respectively.
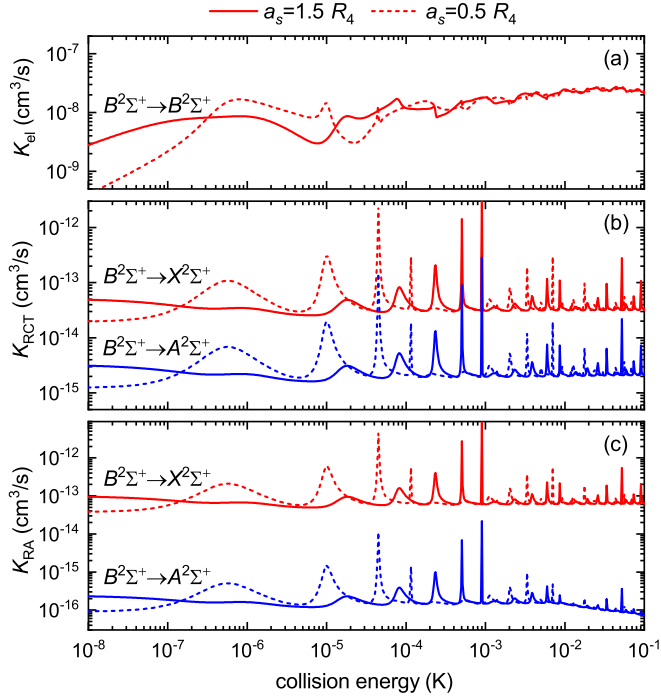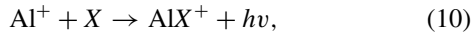
FIG. 7. Rate constants for collisions between the Al^+ ion and Rb atom in the $B\,^2\Sigma^+$ electronic state as a function of the collision energy: (a) elastic scattering, (b) radiative charge transfer, (c) radiative association. Reactive rate constants leading to the $X\,^2\Sigma^+$ and $A\,^2\Pi$ electronic states are shown separately. Results for scattering length set to $0.5R_4$ and $1.5R_4$ are presented.

B. Cold collisions and charge-transfer dynamics

In the considered ion-atom systems there are two paths of collision- and interaction-induced radiative charge rearrangement: (i) the radiative charge transfer (RCT),

$$Al^+ + X \rightarrow Al + X^+ + h\nu, \tag{9}$$
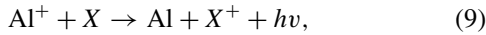
where the electron is spontaneously transferred from the $X =$ Rb(Sr) atom to the Al^+ ion emitting a photon of energy $h\nu$, and (ii) the radiative association (RA),

$$Al^+ + X \rightarrow AlX^+ + h\nu, \tag{10}$$

where the Al^+ ion and the $X =$ Rb(Sr) atom spontaneously form an AlX^+ molecular ion emitting a photon of energy $h\nu$. Scattering of the Al^+ ion with the Rb(Sr) atom is governed by one potential energy curve of the $B\,^2\Sigma^+(B\,^1\Sigma^+)$ symmetry, whereas the charge transfer driven by the transition electric dipole moment can lead to two electronic states of the $X\,^2\Sigma^+$ and $A\,^2\Pi$ ($X\,^1\Sigma^+$ and $A\,^1\Pi$) symmetries, respectively.

Figure 7 presents rate constants for elastic and inelastic reactive collisions between the Al^+ ion and Rb atom as a function of the collision energy. Results for the Al^+ ion and Sr atom have similar energy dependence but the magnitude of rate constants for inelastic collisions is different. Similarly to other ion-atom systems [51,69,72–74], shape resonances are much more pronounced for inelastic rate constants, however, if the thermal Maxwell-Boltzman or Tsallis distribution of collision energies is assumed [75], the thermal averaging removes energy dependence for temperatures larger than 1 mK in agreement with predictions of the classical Langevin

capture theory [76]. Scattering results are presented for two typical scattering lengths ($a_s = 0.5\,R_4$ and $a_s = 1.5\,R_4$) in the entrance channel. Rate constants for small collision energies and pattern of shape resonances depend strongly on these scattering lengths, but the overall magnitude of rate constants does not depend on them. Additionally, all presented results do not depend on the scattering lengths in the exit channels.

In the range of investigated collision energies, the rate constants for the elastic scattering K_{el} for both ion-atom systems have similar values of [see Fig. 7(a)]

$$K_{el}(B\,^2\Sigma^+) \approx K_{el}(B\,^1\Sigma^+) \approx 10^{-8}\,\text{cm}^3/\text{s}.$$

For comparison, the inelastic rate constants given by the classical Langevin capture model determined by the long-range C_4 coefficients $K_L = 2\pi\sqrt{2C_4/\mu}$ [76] take values of $K_L = 3.6 \times 10^{-9}\,\text{cm}^3/\text{s}$ and $K_L = 2.8 \times 10^{-9}\,\text{cm}^3/\text{s}$ for the $Al^+ + $ Rb and $Al^+ + $ Sr systems, respectively.

The rate constants for the inelastic scattering depend strongly on the system and exit electronic state. The rate constants for the radiative charge transfer K_{RCT} for the Al^+ ion colliding with the Rb atom are [see Fig. 7(b)]

$$K_{RCT}(B\,^2\Sigma^+ \rightarrow X\,^2\Sigma^+) \approx 4.5 \times 10^{-14}\,\text{cm}^3/\text{s},$$
$$K_{RCT}(B\,^2\Sigma^+ \rightarrow A^2\Pi) \approx 3 \times 10^{-15}\,\text{cm}^3/\text{s},$$

whereas for the Al^+ ion colliding with the Sr atom they are

$$K_{RCT}(B\,^1\Sigma^+ \rightarrow X\,^1\Sigma^+) \approx 1.4 \times 10^{-17}\,\text{cm}^3/\text{s},$$
$$K_{RCT}(B\,^1\Sigma^+ \rightarrow A^1\Pi) \approx 5 \times 10^{-19}\,\text{cm}^3/\text{s}.$$

Interestingly, the probability of the charge transfer to the $X\,^2\Sigma^+$ state is 15 times larger than to the $A\,^2\Pi$ one in $Al^+ + $ Rb collisions and the probability of the charge transfer to the $X\,^1\Sigma^+$ state is 25 times larger than to the $A\,^1\Pi$ one in $Al^+ + $ Sr collisions. The main reason for observed branching rations is the difference in electric transition dipole moments driving the radiative charge transfer between considered electronic states, which is few times larger for $B \rightarrow X$ transitions as compared to $B \rightarrow A$ ones (see Figs. 4 and 5). The rate constants for spontaneous radiative transitions are proportional to the square of transition dipole moments. Additionally, the probability of the $B \rightarrow X$ and $B \rightarrow A$ charge transfer for $Al^+ + $ Rb collisions is 6000 and 3000 times larger than for $Al^+ + $ Sr collisions, respectively. The main reason for this difference is much smaller energy of emitted photons (the difference of the ionization potentials) in $Al^+ + $ Sr collisions as compared to $Al^+ + $ Rb ones (2346.4 cm^{-1} vs 14587.7 cm^{-1} [63]). The rate constants for spontaneous radiative transitions are proportional to the cubic of the transition energy. The second reason is a larger misalignment of potential wells of the entrance and exit electronic states in the $(Al + Sr)^+$ system as compared to the $(Al + Rb)^+$ one. The rate constants for the nonradiative charge transfer driven by the nonadiabatic radial coupling in $Al^+ + $ Rb ($Al^+ + $ Sr) collisions estimated using the Landau-Zener formula [77] are at least 10 orders (one order) of magnitude smaller than the respective radiative rate constants, in agreement with calculations for other systems [37,69]. Therefore we neglect them in this paper.

The rate constants for the radiative association K_{RA} for the Al$^+$ ion colliding with the Rb atom are [see Fig. 7(c)]

$$K_{RA}(B\,^2\Sigma^+ \to X\,^2\Sigma^+) \approx 9 \times 10^{-14}\,\text{cm}^3/\text{s},$$

$$K_{RA}(B\,^2\Sigma^+ \to A^2\Pi) \approx 2 \times 10^{-16}\,\text{cm}^3/\text{s},$$

whereas for the Al$^+$ ion colliding with the Sr atom they are

$$K_{RA}(B\,^1\Sigma^+ \to X\,^1\Sigma^+) \approx 3.5 \times 10^{-15}\,\text{cm}^3/\text{s},$$

$$K_{RA}(B\,^1\Sigma^+ \to A^1\Pi) \approx 4 \times 10^{-31}\,\text{cm}^3/\text{s}.$$

Interestingly, the probability of the radiative association to the $X\,^2\Sigma^+$ state is 450 times larger than to the $A\,^2\Pi$ one in Al$^+$ + Rb collisions and the radiative association to the $A\,^1\Pi$ state is strongly suppressed in Al$^+$ + Sr collisions. Less favorable transition electric dipole moments for the $B \to A$ association than for the $B \to X$ one are partially responsible for the observed suppression of the rate constants, but the main reason for it is the repulsive character of the $A\,^2\Pi$ and $A\,^1\Pi$ electronic states at intermediate and large distances due to the strongly repulsive nature of the ion-quadruple interaction for Π electronic states and associated small potential well depths (see Fig. 6). Consequently, these electronic states support much smaller number and density of ro-vibrational states as compared to Σ ones (around 10 vibrational levels for $A\,^2\Pi$ and $A\,^1\Pi$ to be compared to around 200 vibrational levels for $X\,^2\Sigma^+$ and $X\,^1\Sigma^+$). Additionally, the short-range classical turning point for the $B\,^1\Sigma^+$ state in the (Al + Sr)$^+$ system overlap with the maximum of the electronic barrier of the $A\,^1\Pi$ state, thus resulting in highly unfavorable Franck-Condon factors. The probability of the $B \to X$ radiative association for Al$^+$ + Rb collisions is only 25 times larger than for Al$^+$ + Sr collisions. For collision energies larger than 10 mK, the rate constants for the $B \to A$ radiative association in both systems start to decrease with increasing collision energy, because the centrifugal barrier in the A electronic states starts to be comparable to the electronic barrier and depth of these states, and suppresses the number of bound ro-vibrational levels which can be populated.

For alkaline-earth-metal ions colliding with alkali-metal atoms, typically, the rate constants for the radiative association are predicted to be significantly larger than the rate constants for the radiative charge transfer [51,74]. In the present case, because of the interplay of the short-range and long-range effects described in the previous paragraphs, the patter is more complex. For the $B \to X$ transition, the radiative association is twice more probable than the radiative charge transfer for Al$^+$ + Rb collisions but the radiative charge transfer is 250 times more probable than the radiative association for Al$^+$ + Sr collisions. For both systems, the $B \to A$ transitions are less probable than the $B \to X$ ones. For the $B \to A$ transition, the radiative charger transfer is 13.5 times more probable than the radiative association for Al$^+$ + Rb collisions and several orders of magnitude more probable for Al$^+$ + Sr collisions.

In the nonrelativistic description of electronic symmetries, the radiative transitions K_R (K_{RA} or K_{RCT}) to the triplet $a\,^3\Pi$ and $b\,^3\Sigma^+$ electronic states in Al$^+$ + Sr collisions are strictly electric dipole forbidden,

$$K_R(B\,^1\Sigma^+ \to a^3\Pi) = K_R(B\,^1\Sigma^+ \to b\,^3\Sigma^+) = 0.$$

The inclusion of the spin-orbit coupling, which is the leading relativistic effect and mixes different nonrelativistic electronic states, slightly modifies the pattern of inelastic rate constants described above.

In Al$^+$ + Rb collisions, the rate constants for the radiative charge transfer and association leading to the $|\Omega| = 3/2$ state are almost the same as they are for transitions leading to the $A\,^2\Pi$ state,

$$K_R((3)1/2 \to (1)3/2) \approx K_R(B\,^2\Sigma^+ \to A^2\Pi),$$

with a small modification due to the change of emitted photons' energy. The relativistic $|\Omega| = 1/2$ electronic states are combinations of the nonrelativistic $X\,^2\Sigma^+$ and $A\,^2\Pi$ states, however, the significant mixing occurs only close to the dissociation threshold whereas the interaction wells of the $(1)1/2$ and $(2)1/2$ states are mostly of the $X\,^2\Sigma^+$ and $A\,^2\Pi$ nature, respectively. The rate constants for the radiative charge transfer and association to the $(1)1/2$ state are within a few percent as compared to the ones to the $X\,^2\Sigma^+$ state in the nonrelativistic picture,

$$K_R((3)1/2 \to (1)1/2) \approx K_R(B\,^2\Sigma^+ \to X\,^2\Sigma^+).$$

The radiative transitions to the $(2)1/2$ state are larger as compared to the ones to the $A\,^2\Pi$ state,

$$K_{RCT}((3)1/2 \to (2)1/2) \approx 2K_{RCT}(B\,^2\Sigma^+ \to A^2\Pi),$$

$$K_{RA}((3)1/2 \to (2)1/2) \approx 3K_{RA}(B\,^2\Sigma^+ \to A^2\Pi),$$

because the spin-orbit coupling and mixing of the $X\,^2\Sigma^+$ and $A\,^2\Pi$ states remove the electronic barrier and repulsive character of the ion-quadruple interaction in the $(2)1/2$ electronic state (see Fig. 6).

The branching ratio of radiative charge-transfer collisions leading to the Al atom in the $^2P_{1/2}$ and $^2P_{3/2}$ fine states is

$$\frac{K_{RCT}(\text{Al}^+ + \text{Rb} \to \text{Al}(^2P_{1/2}) + \text{Rb}^+)}{K_{RCT}(\text{Al}^+ + \text{Rb} \to \text{Al}(^2P_{3/2}) + \text{Rb}^+)} \approx 5.$$

In Al$^+$ + Sr collisions, radiative transitions leading to the $|\Omega| = 2$ state are still electric dipole forbidden,

$$K_R((3)0^+ \to (1)2) = 0,$$

however, the nonrelativistic $a\,^3\Pi$ and $b\,^3\Sigma^+$ electronic states contribute to the relativistic $\Omega = 0^+$ and $|\Omega| = 1$ states.

The relativistic $\Omega = 0^+$ electronic states are combinations of the nonrelativistic $X\,^1\Sigma^+$ and $a\,^3\Pi$ states, but the significant mixing occurs only close to the dissociation threshold whereas the interaction wells of the $(1)0^+$ and $(2)0^+$ states are mostly of the $X\,^1\Sigma^+$ and $a\,^3\Pi$ nature, respectively. The rate constants for the radiative charge transfer to the $(1)0^+$ state is 10 times smaller as compared to the ones to the $X\,^1\Sigma^+$ state in the nonrelativistic picture,

$$K_{RCT}((3)0^+ \to (1)0^+) \approx 0.1 \cdot K_{RCT}(B\,^1\Sigma^+ \to X\,^1\Sigma^+),$$

while the rate constants for the radiative association to the $(1)0^+$ state are just a few percent smaller as compared to the ones to the $X\,^1\Sigma^+$ state,

$$K_{RA}((3)0^+ \to (1)0^+) \approx K_{RA}(B\,^1\Sigma^+ \to X\,^1\Sigma^+).$$

The radiative transitions to the $(2)0^+$ state which is mostly of the $a\,^3\Pi$ nature are possible because of the admixture of the

$X\ ^1\Sigma^+$ state,

$$K_{\mathrm{RCT}}((3)0^+ \to (2)0^+) \approx 0.2 K_{\mathrm{RCT}}(B\ ^1\Sigma^+ \to X\ ^1\Sigma^+),$$

$$K_{\mathrm{RA}}((3)0^+ \to (2)0^+) \approx 0.00005 K_{\mathrm{RA}}(B\ ^1\Sigma^+ \to X\ ^1\Sigma^+).$$

The radiative charge transfer is more affected by the spin-orbit coupling than the radiative association in this case because it is governed by transitions at larger distances where mixing of electronic states and transition moments is larger.

The relativistic $|\Omega| = 1$ electronic states are combinations of the nonrelativistic $A\ ^1\Pi$, $a\ ^3\Pi$, and $b\ ^3\Sigma^+$ states, where similarly as in previous cases, the spin-orbit coupling significantly mixes states close to the dissociation threshold and thus affects more the charge transfer. Additionally, the wells of the (1)1 and (2)1 states are mixtures of the crossing $a\ ^3\Pi$ and $b\ ^3\Sigma^+$ states, whereas the interaction well of the (3)1 state is mostly of the $A\ ^1\Pi$ nature. The resulting rate constants for the radiative charge transfer are

$$K_{\mathrm{RCT}}((3)0^+ \to (1)1) \approx 0.002 K_{\mathrm{RCT}}(B\ ^1\Sigma^+ \to A^1\Pi),$$

$$K_{\mathrm{RCT}}((3)0^+ \to (2)1) \approx 0.15 K_{\mathrm{RCT}}(B\ ^1\Sigma^+ \to A^1\Pi),$$

$$K_{\mathrm{RCT}}((3)0^+ \to (3)1) \approx 0.8 K_{\mathrm{RCT}}(B\ ^1\Sigma^+ \to A^1\Pi),$$

while the rate constants for the radiative association are

$$K_{\mathrm{RA}}((3)0^+ \to (1)1) \approx 2.2 K_{\mathrm{RCT}}((3)0^+ \to (1)1),$$

$$K_{\mathrm{RA}}((3)0^+ \to (2)1) \approx 0.2 K_{\mathrm{RCT}}((3)0^+ \to (2)1),$$

$$K_{\mathrm{RA}}((3)0^+ \to (3)1) \approx 10^{-8} \times K_{\mathrm{RCT}}((3)0^+ \to (3)1).$$

The branching ratio of radiative charge-transfer collisions leading to the Al atom in the $^2P_{1/2}$ and $^2P_{3/2}$ fine states is

$$\frac{K_{\mathrm{RCT}}(\mathrm{Al}^+ + \mathrm{Sr} \to \mathrm{Al}(^2P_{1/2}) + \mathrm{Sr}^+)}{K_{\mathrm{RCT}}(\mathrm{Al}^+ + \mathrm{Sr} \to \mathrm{Al}(^2P_{3/2}) + \mathrm{Sr}^+)} \approx \frac{1}{2}.$$

Finally, all calculated rate constants for the radiative charge transfer and association are significantly smaller (at least 10^4 times smaller) than the Langevin rate constants. This means that at least 10^4 collisions is needed to observe reactive processes in the $\mathrm{Al}^+ + \mathrm{Rb}$ and $\mathrm{Al}^+ + \mathrm{Sr}$ systems. In typical hybrid ion-atom experiments measuring such small rate constants is challenging because long interrogation times are needed. The employment of the precision measurement within the generalized quantum logic spectroscopy scheme, where an alkaline-earth-metal ion is used to monitor the replacement of the Al^+ ion by $\mathrm{Rb}^+(\mathrm{Sr}^+)$ or $\mathrm{AlRb}^+(\mathrm{AlSr}^+)$ and their energy, may allow one to assess statistics of these relatively rare events due to enhanced controllability and sensitivity of such a scheme [78,79]. On the other hand, small reactivity can be an advantage providing long interrogation times to probe even weak ion-atom interactions. The measurement of the charge and energy transfer on the single-collision level can also be envisioned [42,80]. In fact, sympathetic cooling in the considered ion-atom systems may be challenging due to the micromotion-induced heating [81]. On the other hand, recent developments on optical ion trapping may be a remedy [82,83].

C. Formation and control of molecular ions

In the previous subsection, we have analyzed the branching ratios of the radiative association to different electronic states and showed that formation of molecular ions is more probable
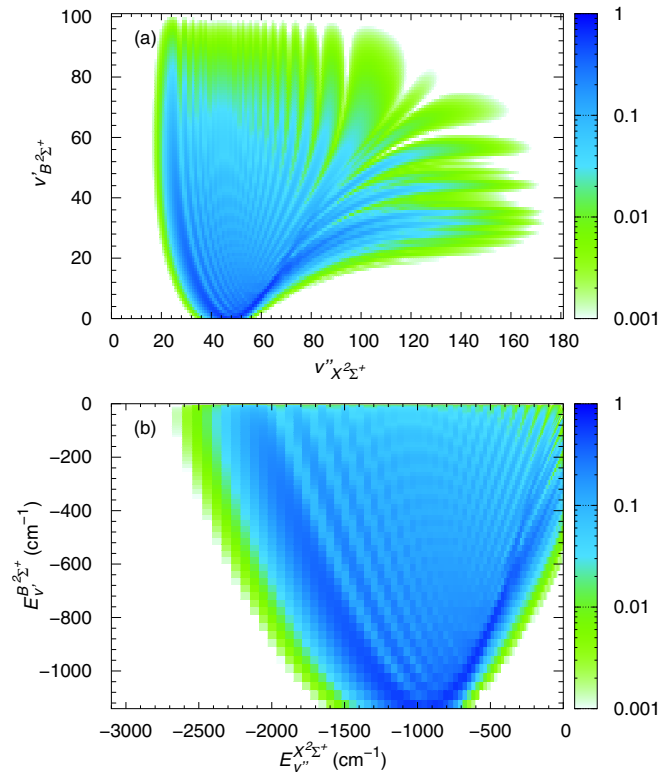

FIG. 8. Transition electric dipole moments between vibrational levels of the $X\ ^2\Sigma^+$ ground and $B\ ^2\Sigma^+$ excited electronic states of the $(\mathrm{Al} + \mathrm{Rb})^+$ ion-atom system as a function of the vibrational quantum numbers (a) and vibrational energies (b).

in the $X\ ^2\Sigma^+$ and $X\ ^1\Sigma^+$ (and related relativistic) states than in the $A\ ^2\Sigma^+$ and $A\ ^1\Sigma^+$ ones in $\mathrm{Al}^+ + \mathrm{Rb}$ and $\mathrm{Al}^+ + \mathrm{Sr}$ collisions, respectively. Now, we investigate the branching ratios to different vibrational levels of the ground electronic states. Figure 8 presents the transition electric dipole moments between vibrational levels of the $X\ ^2\Sigma^+$ ground and $B\ ^2\Sigma^+$ excited electronic states of the $(\mathrm{Al} + \mathrm{Rb})^+$ ion-atom system as a function of the vibrational quantum numbers in the upper panel and vibrational energies in the bottom panel. These transition dipole moments govern both spontaneous and stimulated transitions between different vibrational levels. The presented map of the transition electric dipole moments can be useful to engineer molecular ions in selected vibrational levels. Similar calculations were realized for the $(\mathrm{Al} + \mathrm{Sr})^+$ ion-atom system and other electronic states in both nonrelativistic and relativistic pictures. Unfortunately, there is no efficient path for the formation of the absolute ground-state molecular ions using the B and X electronic states.

Radiative association rate constants as a function of the energy of the final ro-vibrational level in the $X\ ^2\Sigma^+$ electronic ground state for the Al^+ ion colliding with the Rb atom in the $B\ ^2\Sigma^+$ state are plotted in Fig. 9. In $\mathrm{Al}^+ + \mathrm{Rb}$ collisions, the formation of molecular ions in vibrational levels with the vibrational quantum number around $v = 24$ and the binding energy around $2155\ \mathrm{cm}^{-1}$ of the $X\ ^2\Sigma^+$ electronic state is the most probable. In $\mathrm{Al}^+ + \mathrm{Sr}$ collisions, the formation of molecular ions in vibrational levels with the vibrational quantum number around $v = 88$ and the binding
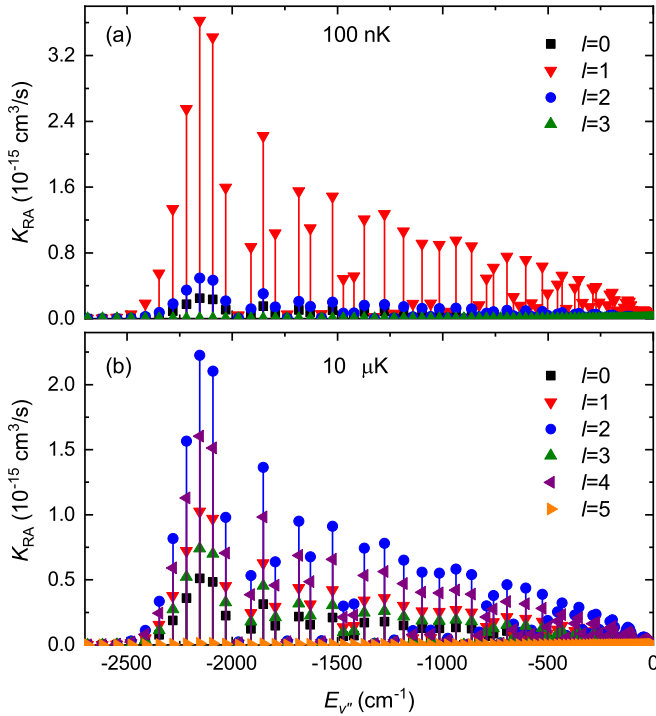
FIG. 9. Radiative association rate constants as a function of the energy of the final ro-vibrational level in the X $^2\Sigma^+$ electronic ground state of the AlRb$^+$ molecular ion for the Al$^+$ ion colliding with the Rb atom in the B $^2\Sigma^+$ state with the scattering length of R_4 at the temperature of 100 nK (a) and 10 μK (b).

energy around $1709\,\mathrm{cm}^{-1}$ of the X $^1\Sigma^+$ electronic state is the most probable. In both systems, the molecular formation probability decreases gradually for decreasing binding energies and is strongly suppressed for binding energies larger than $2500\,\mathrm{cm}^{-1}$. In both systems, the formation of molecular ions in the A electronic states is the most probable in the last and most-weakly bound vibrational level due to the suppression described in the previous subsection. Collisions at temperature of 100 nK in Fig. 9(a) are dominated by s wave, therefore, molecular ions in the first excited rotational state ($l = 1$) are mostly formed. At temperature of 10 μK in Fig. 9(b) several partial waves already contribute in collisions, therefore, a broader range of rotational molecular states is populated.

In all considered cases of the radiative association, the formation of deeply bound molecular ions close the the ground vibrational level $v = 0$ is strongly suppressed due to the misalignment of the potential wells of the entrance B and exit X and A electronic states. To overcome this problem and to enable the formation of ground-state molecular ions with larger binding energies, the two-photon schemes using an intermediate electronic state can be employed [84]. In such scenarios, colliding ion-atom pairs can be excited to a selected intermediate excited electronic state, which has better overlaps with both the initial B and final X and A states. Next, spontaneous or stimulated emission can result in the formation of deeply bound molecular ions. For the $(\mathrm{Al} + \mathrm{Rb})^+$ and $(\mathrm{Al} + \mathrm{Sr})^+$ ion-atom systems, the D $^2\Pi$ and (3) $^1\Pi$ excited electronic state can be used as intermediate states in the two-photon formation, respectively. After the initial spontaneous or stimulated radiative association, the stabilization to the

ground vibrational level can also be realized with two-photon schemes using stimulated Raman adiabatic passage (STIRAP) [85]. The quantum logic spectroscopy can also be used for state-selective detection of formed molecular ions based on different rotational consonants and dipole moments of molecular ions in different vibrational states [86,87].

IV. SUMMARY AND CONCLUSIONS

Motivated by recent experimental advances on highly precise atomic clocks based on sympathetically cooled Al$^+$ ions, on one hand, and on the preparation and application of cold ion-atom systems, on the other hand, here we have proposed to employ an Al$^+$ ion co-trapped in a Paul trap with a laser-cooled alkaline-earth-metal ion and overlapped with a small cloud of ulracold Rb or Sr atoms to probe ulracold ion-atom interactions and collisions, including radiative charge exchange and association processes.

We have calculated potential energy curves and transition electric dipole moments for the prototype $(\mathrm{Al} + \mathrm{Rb})^+$ and $(\mathrm{Al} + \mathrm{Sr})^+$ ion-atom systems using state-of-the-art *ab initio* electronic structure techniques of quantum chemistry such as the coupled cluster and multireference configuration interaction methods with scalar relativistic effects included within the small-core energy-consistent pseudopotentials. We have also used perturbation theory to obtain the long-range interaction coefficients and to include the relativistic spin-orbit coupling between nonrelativistic molecular electronic states. Next, the electronic structure data have been employed to investigate cold collisions and charge-transfer dynamics.

Scattering of an Al$^+$ ion with alkali-metal or alkaline-earth-metal atom is governed by a single potential energy curve whereas dipole allowed transitions can lead to several electronic states mixed by the spin-orbit coupling. Such transitions can result in the radiative charge transfer or radiative association. We have analyzed the interplay of the short-range and long-range effects, and examined the branching ratios for those rich and interesting processes. We have also investigated the prospects for the laser-field control and formation of molecular ions.

The atomic clock transition in an Al$^+$ ion can be employed to monitor ion-atom interactions and scattering dynamics *via* quantum logic spectroscopy [7]. In this method, the quantum state detection and preparation of the Al$^+$ ion can be realized by optical addressing of a co-trapped alkaline-earth-metal ion. The frequency shift of trapped-ion optical clocks caused by background-gas collisions has recently been actively studied [88–92]. High precision measurement of the narrow clock transition may allow one to probe even weak ion-atom interactions and long interrogation times may allow one to assess statistics of relatively rare events of charge-transfer collisions [78,79]. The charge and energy transfer may also potentially be investigated on the single-collision level [80]. In summary, the presented results pave the way for the application of ions other than alkali-metal and alkaline-earth-metal ones in the field of cold hybrid ion-atom experiments.

[1] D. J. Wineland, Rev. Mod. Phys. **85**, 1103 (2013).

[2] H. Haeffner, C. F. Roos, and R. Blatt, Phys. Rep. **469**, 155 (2008).

[3] R. Blatt and C. Roos, Nat. Phys. **8**, 277 (2012).

[4] D. J. Wineland, J. C. Bergquist, J. J. Bollinger, R. E. Drullinger, and W. M. Itano, in *Proceedings of the 6th Symposium on Frequency Standards and Metrology* (World Scientific, Singapore, 2002).

[5] C. L. Degen, F. Reinhard, and P. Cappellaro, Rev. Mod. Phys. **89**, 035002 (2017).

[6] M. G. Kozlov, M. S. Safronova, J. R. Crespo López-Urrutia, and P. O. Schmidt, Rev. Mod. Phys. **90**, 045005 (2018).

[7] P. O. Schmidt, T. Rosenband, C. Langer, W. M. Itano, J. C. Bergquist, and D. J. Wineland, Science **309**, 749 (2005).

[8] T. Rosenband, D. B. Hume, P. O. Schmidt, C. W. Chou, A. Brusch, L. Lorini, W. H. Oskay, R. E. Drullinger, T. M. Fortier, J. E. Stalnaker, S. A. Diddams, W. C. Swann, N. R. Newbury, W. M. Itano, D. J. Wineland, and J. C. Bergquist, Science **319**, 1808 (2008).

[9] C. W. Chou, D. B. Hume, J. C. J. Koelemeij, D. J. Wineland, and T. Rosenband, Phys. Rev. Lett. **104**, 070802 (2010).

[10] N. Huntemann, C. Sanner, B. Lipphardt, C. Tamm, and E. Peik, Phys. Rev. Lett. **116**, 063001 (2016).

[11] J.-S. Chen, S. M. Brewer, C. W. Chou, D. J. Wineland, D. R. Leibrandt, and D. B. Hume, Phys. Rev. Lett. **118**, 053002 (2017).

[12] S. M. Brewer, J.-S. Chen, A. M. Hankin, E. R. Clements, C. W. Chou, D. J. Wineland, D. B. Hume, and D. R. Leibrandt, Phys. Rev. Lett. **123**, 033201 (2019).

[13] A. Härter and J. H. Denschlag, Contemp. Phys. **55**, 33 (2014).

[14] R. Côté, Adv. At. Mol. Opt. Phys. **65**, 67 (2016).

[15] M. Tomza, K. Jachymski, R. Gerritsma, A. Negretti, T. Calarco, Z. Idziaszek, and P. S. Julienne, Rev. Mod. Phys. **91**, 035001 (2019).

[16] I. Bloch, J. Dalibard, and W. Zwerger, Rev. Mod. Phys. **80**, 885 (2008).

[17] C. Gross and I. Bloch, Science **357**, 995 (2017).

[18] R. Côté and A. Dalgarno, Phys. Rev. A **62**, 012709 (2000).

[19] C. Zipkes, S. Palzer, C. Sias, and M. Köhl, Nature (London) **464**, 388 (2010).

[20] K. Ravi, S. Lee, A. Sharma, G. Werth, and S. Rangwala, Nat. Commun. **3**, 1126 (2012).

[21] B. Höltkemeier, P. Weckesser, H. López-Carrera, and M. Weidemüller, Phys. Rev. Lett. **116**, 233003 (2016).

[22] A. Petrov, C. Makrides, and S. Kotochigova, J. Chem. Phys. **146**, 084304 (2017).

[23] T. Feldker, H. Fürst, H. Hirzler, N. Ewald, M. Mazzanti, D. Wiater, M. Tomza, and R. Gerritsma, Nat. Phys. (2020), doi: 10.1038/s41567-019-0772-5.

[24] F. H. J. Hall and S. Willitsch, Phys. Rev. Lett. **109**, 233202 (2012).

[25] O. P. Makarov, R. Côté, H. Michels, and W. W. Smith, Phys. Rev. A **67**, 042705 (2003).

[26] L. Ratschbacher, C. Zipkes, C. Sias, and M. Kohl, Nat. Phys. **8**, 649 (2012).

[27] H. Fürst, T. Feldker, N. V. Ewald, J. Joger, M. Tomza, and R. Gerritsma, Phys. Rev. A **98**, 012713 (2018).

[28] T. Sikorsky, M. Morita, Z. Meir, A. A. Buchachenko, R. Ben-shlomi, N. Akerman, E. Narevicius, T. V. Tscherbul, and R. Ozeri, Phys. Rev. Lett. **121**, 173402 (2018).

[29] R. Côté and I. Simbotin, Phys. Rev. Lett. **121**, 173401 (2018).

[30] R. Saito, S. Haze, M. Sasakawa, R. Nakai, M. Raoult, H. Da Silva, O. Dulieu, and T. Mukaiyama, Phys. Rev. A **95**, 032709 (2017).

[31] T. Sikorsky, Z. Meir, R. Ben-shlomi, N. Akerman, and R. Ozeri, Nat. Commun. **9**, 920 (2018).

[32] U. Bissbort, D. Cocks, A. Negretti, Z. Idziaszek, T. Calarco, F. Schmidt-Kaler, W. Hofstetter, and R. Gerritsma, Phys. Rev. Lett. **111**, 080501 (2013).

[33] H. Doerk, Z. Idziaszek, and T. Calarco, Phys. Rev. A **81**, 012708 (2010).

[34] A. T. Grier, M. Cetina, F. Oručević, and V. Vuletić, Phys. Rev. Lett. **102**, 223201 (2009).

[35] F. H. Hall, P. Eberle, G. Hegi, M. Raoult, M. Aymar, O. Dulieu, and S. Willitsch, Mol. Phys. **111**, 2020 (2013).

[36] S. T. Sullivan, W. G. Rellergert, S. Kotochigova, and E. R. Hudson, Phys. Rev. Lett. **109**, 223002 (2012).

[37] W. G. Rellergert, S. T. Sullivan, S. Kotochigova, A. Petrov, K. Chen, S. J. Schowalter, and E. R. Hudson, Phys. Rev. Lett. **107**, 243201 (2011).

[38] S. Haze, S. Hata, M. Fujinaga, and T. Mukaiyama, Phys. Rev. A **87**, 052715 (2013).

[39] F. H. J. Hall, M. Aymar, N. Bouloufa-Maafa, O. Dulieu, and S. Willitsch, Phys. Rev. Lett. **107**, 243202 (2011).

[40] W. Smith, D. Goodman, I. Sivarajah, J. Wells, S. Banerjee, R. Côté, H. Michels, J. A. Mongtomery, and F. Narducci, Appl. Phys. B **114**, 75 (2014).

[41] J. Joger, H. Fürst, N. Ewald, T. Feldker, M. Tomza, and R. Gerritsma, Phys. Rev. A **96**, 030703(R) (2017).

[42] Z. Meir, T. Sikorsky, R. Ben-shlomi, N. Akerman, Y. Dallal, and R. Ozeri, Phys. Rev. Lett. **117**, 243401 (2016).

[43] A. Härter, A. Krükow, A. Brunner, W. Schnitzler, S. Schmid, and J. H. Denschlag, Phys. Rev. Lett. **109**, 123201 (2012).

[44] J. Deiglmayr, A. Göritz, T. Best, M. Weidemüller, and R. Wester, Phys. Rev. A **86**, 043438 (2012).

[45] S. Jyothi, T. Ray, S. Dutta, A. R. Allouche, R. Vexiau, O. Dulieu, and S. A. Rangwala, Phys. Rev. Lett. **117**, 213002 (2016).

[46] K. S. Kleinbach, F. Engel, T. Dieterle, R. Löw, T. Pfau, and F. Meinert, Phys. Rev. Lett. **120**, 193401 (2018).

[47] T. Schmid, C. Veit, N. Zuber, R. Löw, T. Pfau, M. Tarana, and M. Tomza, Phys. Rev. Lett. **120**, 153401 (2018).

[48] M. Tomza, Phys. Rev. A **92**, 062701 (2015).

[49] M. Tomza, F. Pawlowski, M. Jeziorska, C. P. Koch, and R. Moszynski, Phys. Chem. Chem. Phys. **13**, 18893 (2011).

[50] M. Tomza, M. H. Goerz, M. Musiał, R. Moszynski, and C. P. Koch, Phys. Rev. A **86**, 043424 (2012).

[51] M. Tomza, C. P. Koch, and R. Moszynski, Phys. Rev. A **91**, 042706 (2015).

[52] H. Werner and P. J. Knowles, J. Chem. Phys. **89**, 5803 (1988).

[53] P. J. Knowles, C. Hampel, and H.-J. Werner, J. Chem. Phys. **99**, 5219 (1993).

[54] S. Boys and F. Bernardi, Mol. Phys. **19**, 553 (1970).

[55] D. E. Woon and T. H. Dunning, Jr., J. Chem. Phys. **98**, 1358 (1993).

[56] M. Dolg and X. Cao, Chem. Rev. **112**, 403 (2012).

[57] I. S. Lim, P. Schwerdtfeger, B. Metz, and H. Stoll, J. Chem. Phys. **122**, 104103 (2005).

[58] I. S. Lim, H. Stoll, and P. Schwerdtfeger, J. Chem. Phys. **124**, 034107 (2006).

[59] M. Tomza, W. Skomorowski, M. Musial, R. Gonzalez Ferez, C. P. Koch, and R. Moszynski, Mol. Phys. **111**, 1781 (2013).

[60] F.-M. Tao and Y.-K. Pan, J. Chem. Phys. **97**, 4989 (1992).

[61] H.-J. Werner, P. J. Knowles, G. Knizia, F. R. Manby, M. Schütz, P. Celani, T. Korona, R. Lindh, A. Mitrushenkov, G. Rauhut, K. R. Shamasundar, T. B. Adler, R. D. Amos, A. Bernhardsson, A. Berning, D. L. Cooper, M. J. O. Deegan, A. J. Dobbyn, F. Eckert, E. Goll, C. Hampel, A. Hesselmann, G. Hetzer, T. Hrenar, G. Jansen, C. Köppl, Y. Liu, A. W. Lloyd, R. A. Mata, A. J. May, S. J. McNicholas, W. Meyer, M. E. Mura, A. Nicklass, D. P. O'Neill, P. Palmieri, D. Peng, K. Pflüger, R. Pitzer, M. Reiher, T. Shiozaki, H. Stoll, A. J. Stone, R. Tarroni, T. Thorsteinsson, and M. Wang, Computer code MOLPRO, Version 2012.1, a package of *ab initio* programs, 2012, http://www.molpro.net.

[62] K. G. Dyall and K. Fægri, Jr., *Introduction to Relativistic Quantum Chemistry* (Oxford University Press, Oxford, 2007).

[63] NIST Atomic Spectra Database, http://physics.nist.gov/PhysRefData/ASD.

[64] B. Jeziorski, R. Moszynski, and K. Szalewicz, Chem. Rev. **94**, 1887 (1994).

[65] A. Derevianko, S. G. Porsev, and J. F. Babb, At. Data Nucl. Data Tables **96**, 323 (2010).

[66] T. Korona, M. Przybytek, and B. Jeziorski, Mol. Phys. **104**, 2303 (2006).

[67] M. Tomza, R. González-Férez, C. P. Koch, and R. Moszynski, Phys. Rev. Lett. **112**, 113201 (2014).

[68] B. R. Johnson, J. Chem. Phys. **69**, 4678 (1978).

[69] E. R. Sayfutyarova, A. A. Buchachenko, S. A. Yakovleva, and A. K. Belyaev, Phys. Rev. A **87**, 052717 (2013).

[70] M. Li, M. Mills, P. Puri, A. Petrov, E. R. Hudson, and S. Kotochigova, Phys. Rev. A **99**, 062706 (2019).

[71] J. Mitroy, M. S. Safronova, and C. W. Clark, J. Phys. B: At. Mol. Opt. Phys. **43**, 202001 (2010).

[72] M. Krych, W. Skomorowski, F. Pawłowski, R. Moszynski, and Z. Idziaszek, Phys. Rev. A **83**, 032723 (2011).

[73] Z. Idziaszek, A. Simoni, T. Calarco, and P. S. Julienne, New J. Phys. **13**, 083005 (2011).

[74] H. da Silva, Jr., M. Raoult, M. Aymar, and O. Dulieu, New J. Phys. **17**, 045015 (2015).

[75] I. Rouse and S. Willitsch, Phys. Rev. Lett. **118**, 143401 (2017).

[76] R. D. Levine, *Molecular Reaction Dynamics* (Cambridge University Press, Cambridge, 2009).

[77] A. K. Belyaev and O. V. Lebedev, Phys. Rev. A **84**, 014701 (2011).

[78] S. M. Brewer, J.-S. Chen, K. Beloy, A. M. Hankin, E. R. Clements, C. W. Chou, W. F. McGrew, X. Zhang, R. J. Fasano, D. Nicolodi, H. Leopardi, T. M. Fortier, S. A. Diddams, A. D. Ludlow, D. J. Wineland, D. R. Leibrandt, and D. B. Hume, Phys. Rev. A **100**, 013409 (2019).

[79] M. Guggemos, M. Guevara-Bertsch, D. Heinrich, O. A. Herrera-Sancho, Y. Colombe, R. Blatt, and C. F. Roos, New J. Phys. **21**, 103003 (2019).

[80] Z. Meir, M. Pinkas, T. Sikorsky, R. Ben-shlomi, N. Akerman, and R. Ozeri, Phys. Rev. Lett. **121**, 053402 (2018).

[81] M. Cetina, A. T. Grier, and V. Vuletić, Phys. Rev. Lett. **109**, 253201 (2012).

[82] J. Schmidt, P. Weckesser, F. Thielemann, T. Schaetz, and L. Karpa, arXiv:1909.8352 [Phys. Rev. Lett. (to be published)].

[83] C. Schneider, M. Enderlein, T. Huber, and T. Schaetz, Nat. Photon. **4**, 772 (2010).

[84] M. Gacesa, J. A. Montgomery, H. H. Michels, and R. Côté, Phys. Rev. A **94**, 013407 (2016).

[85] N. V. Vitanov, A. A. Rangelov, B. W. Shore, and K. Bergmann, Rev. Mod. Phys. **89**, 015006 (2017).

[86] K. Chen, S. J. Schowalter, S. Kotochigova, A. Petrov, W. G. Rellergert, S. T. Sullivan, and E. R. Hudson, Phys. Rev. A **83**, 030501(R) (2011).

[87] F. Wolf, Y. Wan, J. C. Heip, F. Gebert, C. Shi, and P. O. Schmidt, Nature (London) **530**, 457 (2016).

[88] K. Gibble, Phys. Rev. Lett. **110**, 180802 (2013).

[89] A. C. Vutha, T. Kirchner, and P. Dubé, Phys. Rev. A **96**, 022704 (2017).

[90] A. Vutha, T. Kirchner, and P. Dubé, arXiv:1812.00973.

[91] A. M. Hankin, E. R. Clements, Y. Huang, S. M. Brewer, J.-S. Chen, C. W. Chou, D. B. Hume, and D. R. Leibrandt, Phys. Rev. A **100**, 033419 (2019).

[92] J. Davis, P. Dubé, and A. C. Vutha, Phys. Rev. Research **1**, 033137 (2019).